INTERNATIONAL JOURNAL FOR NUMERICAL METHODS IN FLUIDS
Int. J. Numer. Meth. Fluids 2004; **46**:507–532 (DOI: 10.1002/fld.765)

Coupled lattice-Boltzmann and finite-difference simulation of electroosmosis in microfluidic channels

Dzmitry Hlushkou[1], Drona Kandhai[2] and Ulrich Tallarek[3,*,†]

[1] *Max-Planck-Institut für Dynamik komplexer technischer Systeme, Sandtorstraße 1, 39106 Magdeburg, Germany*
[2] *Kramers Laboratorium voor Fysische Technologie, Delft University of Technology, Prins Bernhardlaan 6, 2628 BW Delft, The Netherlands*
[3] *Institut für Verfahrenstechnik, Otto-von-Guericke-Universität Magdeburg, Universitätsplatz 2, 39106 Magdeburg, Germany*

SUMMARY

In this article we are concerned with an extension of the lattice-Boltzmann method for the numerical simulation of three-dimensional electroosmotic flow problems in porous media. Our description is evaluated using simple geometries as those encountered in open-channel microfluidic devices. In particular, we consider electroosmosis in straight cylindrical capillaries with a (non)uniform zeta-potential distribution for ratios of the capillary inner radius to the thickness of the electrical double layer from 10 to 100. The general case of heterogeneous zeta-potential distributions at the surface of a capillary requires solution of the following coupled equations in three dimensions: Navier–Stokes equation for liquid flow, Poisson equation for electrical potential distribution, and the Nernst–Planck equation for distribution of ionic species. The hydrodynamic problem has been treated with high efficiency by code parallelization through the lattice-Boltzmann method. For validation velocity fields were simulated in several microcapillary systems and good agreement with results predicted either theoretically or obtained by alternative numerical methods could be established. Results are also discussed with respect to the use of a slip boundary condition for the velocity field at the surface. Copyright © 2004 John Wiley & Sons, Ltd.

KEY WORDS: lattice-Boltzmann method; finite-difference method; porous media; microfluidics; electroosmotic flow; surface charge distribution

1. INTRODUCTION

Rapid recent developments in design, patterning, and utilization of microfluidic devices (valves, pumps, mixers, reactors, sensors and actuators, or three-dimensional channel networks) have

*Correspondence to: U. Tallarek, Institut für Verfahrenstechnik, Otto-von-Guericke-Universität Magdeburg, Universitätsplatz 2, 39106 Magdeburg, Germany.
†E-mail: ulrich.tallarek@vst.uni-magdeburg.de

Published online 18 August 2004

Received 7 October 2003
Revised 30 April 2004

found many applications in the devised bulk transport and separation, identification, synthesis, and manipulation of a wide range of chemical and biological species [1–6]. It is an advancement that becomes particularly important for the lab-on-a-chip concept [7] where transport processes including the efficient mixing of micro- and nanoliter liquid volumes, the control and enhancement of reaction rates, heat and mass transfer, as well as the selectivity of chromatographic separations occur on much smaller time and length scales than traditional engineering technologies. With channel diameters from several to a few hundred micrometers (inherently placing microfluidics into the low-Reynolds number hydrodynamics regime) and channel lengths approaching centimeter dimension, these systems permit a miniaturization of chemical processes and large-scale integration of engineering principles, allowing fast response times at low operational costs [6].

Concerning the bulk transport of liquid through a microfluidic channel electroosmosis can offer distinct advantages over pressure-driven flow. Electroosmotic flow (EOF) is generated by interaction of an externally applied electrical field with that part of the electrolyte solution that has become locally charged at the interface to the stationary and oppositely charged solid surface of the confining porous medium [8, 9]. The extension into the bulk solution of the fluid-side domain of this electrical double layer can be as small as a few nanometers compared to a channel diameter of micrometer dimension, a fact that has some important consequences for the EOF dynamics under these conditions [10]. First, from a macroscopic point of view, bulk liquid moves as in plug flow, i.e. the velocity apparently slips at the wall, which is in contrast to the parabolic velocity profile typical for Poiseuille flow. Second, because the ratio of electroosmotic to hydraulic volumetric flow rates (at fixed potential and pressure gradient) is inversely proportional to the squared channel diameter, the EOF becomes increasingly effective in liquid transport through the finer channels as their size is reduced. Thus the benefit of using EOF is that chemical and biological species may be easily transported in microfluidic devices over comparatively long distances with negligible mass transfer resistance. Hydrodynamic dispersion can then be limited almost to that by longitudinal diffusion alone which has been demonstrated experimentally [11, 12].

Stimulated by the enormous potential and accompanying need for a far more detailed characterization of the electrokinetically driven mass transport in microfabricated (or microchip) devices, numerical simulation of EOF in microfluidic channels has received increased attention over the past few years [13–28]. These investigations have revealed that, in good agreement with available experimental data, the transport characteristics of the EOF in microchannels clearly depend on the properties of the working fluid and the geometrical (and physico-chemical) parameters of the surface. For example, the work of Griffiths and Nilson [16] which is based on a direct solution of the governing transport equations demonstrates that, over a wide range of conditions, the longitudinal dispersion coefficient of a neutral, non-reacting solute in EOF may be many orders of magnitude smaller than for the parabolic or nearly so velocity distribution in pressure-driven flow. Ermakov *et al.* [15] used a 2D code to address the electrokinetic species transport with respect to some basic microfluidic elements. They considered the sample focusing in a channel cross and sample mixing at a T-junction. Patankar and Hu [14] carried out 3D flow field simulations to investigate EOF behaviour at a channel cross, while Bianchi *et al.* [17] used finite element-based simulations to describe flow division at a decoupling T-junction, encountering combined electroosmotic and pressure-driven flows. Fu *et al.* [25] presented a physical model and numerical method for studying geometrical effects on the performance of electrophoresis microchips. Erickson

and Li [27] utilized 3D finite element-based numerical simulations to resolve the influence of a heterogeneous surface charge distribution on local flow circulation in the bulk liquid under the aspect of sample mixing in a T-shaped micromixer. While these numerical approaches provide valuable insight into flow behaviour in relatively simple channel geometries, traditional computational fluid dynamics can face drawbacks if higher code flexibility is required, e.g. when dealing with a more complicated pore space morphology, complex flows, or code parallelization.

Over the last decade the lattice-Boltzmann (LB) methods [29–34] have achieved great success as alternative and efficient numerical schemes in the simulation of a variety of transport phenomena in porous media, with a particular emphasis on the dynamics of pressure-driven fluid flow through complex materials [34–50]. Besides their flexibility and accuracy in dealing with the confining geometry and actual boundary conditions LB methods are inherently parallel and, thus, they are ideally suited for high-performance parallel computing. In contrast to the more conventional numerical schemes based on a discretization of macroscopic continuum equations, the LB method utilizes mesoscopic kinetic equations to recover the macroscopic Navier–Stokes equation for fluid motion in the long-time, large-scale limit [34]. Further, early systematic problems of LB methods like the existence of velocity-dependent pressures and lack of a Galilean invariance are essentially resolved, and algorithms have been simplified by the single relaxation time scheme of Bhatnagar *et al.* [51–53].

Only a few reports have been published so far in which LB simulations also consider electrokinetic phenomena. Rather recently, the LB method has been implemented to model high-Reynolds number pressure-driven flow in microfluidics, taking into account electroviscous effects that can become important due to the finite thickness of electrical double layers compared to typical channel sizes [54], and a reasonable agreement with published experimental data on the friction factor—Reynolds number relation [55] was obtained. Further, in the work by Nie *et al.* [56] an extension of the LB method was proposed based on a density-dependent viscosity model and technique for imposing a slip-velocity at the wall. It was demonstrated that this approach can capture fundamental characteristics of microchannel flow. Warren [57] analysed electrokinetic transport in a parallel-sided slit with a constant electrical charge (or potential) at this solid–liquid interface. The resulting one-dimensional problem was further restrained by assuming a thick electrical double layer compared to the width of the slit. While this work addresses cases with significant double layer overlap encountered in ultrafine capillaries [58], for many situations with technological relevance, as for the electrokinetic transport in open-channel microchip devices, a characteristic channel dimension normal to the local flow direction becomes (much) larger than the typical thickness of electrical double layers at the solid–liquid interface. It is this condition, in particular, that needs to be satisfied in order to gain full potential of the EOF (compared to pressure-driven flow) with respect to dispersion and permeability [59]. Further, most industrial and natural porous media are characterized by random or hierarchically-structured, but relatively broad pore size distributions, contrasting with the network of uniformly sized and shaped channels in microfluidic devices. In the general case, bulk transport involves conditions for which the ratio of a local pore radius to the electrical double layer thickness covers a spectrum from below unity up to several hundreds [60]. The numerical approach that we present in this work can cope with any geometry and possible surface heterogeneity and, thus, it will be particularly efficient in resolving details of the flow field that govern transport and dispersion in a transient, as well as long-time asymptotic regime.

2. ELECTROKINETICS

2.1. Electroosmotic flow in a microfluidic channel

Figure 1 illustrates, at different length scales, the basic aspects of electroosmosis in a microfluidic channel with locally flat, smooth surface. When a dielectric solid (e.g. a fused-silica capillary) is contacted with a liquid electrolyte (e.g. a dilute aqueous NaCl solution) an electrical double layer (EDL) developes at the solid–liquid interface due to ionizable groups of the material (dissociation of silanol groups in the above example: $\equiv Si-OH+H_2O \Leftrightarrow \equiv Si-O^- + H_3O^+$) or by ions adsorbing on its surface. The resulting negative charge density of the capillary (channel) inner wall affects the distribution of hydrated sodium (counter)ions in the solution: In immediate proximity to the surface there exists a layer of ions which are relatively strongly fixed by electrostatic forces. It forms the inner or compact part of the fluid-side domain of the EDL and its typical thickness is of the order of only one ion diameter (about 0.5 nm). The outer Helmholtz plane (OHP, Figure 1(c)) separates inner and diffusive layers which, together, constitute the EDL. While the ionic species in the diffusive layer undergo Brownian motion, they are also influenced by the local electrostatic potential. At equilibrium their

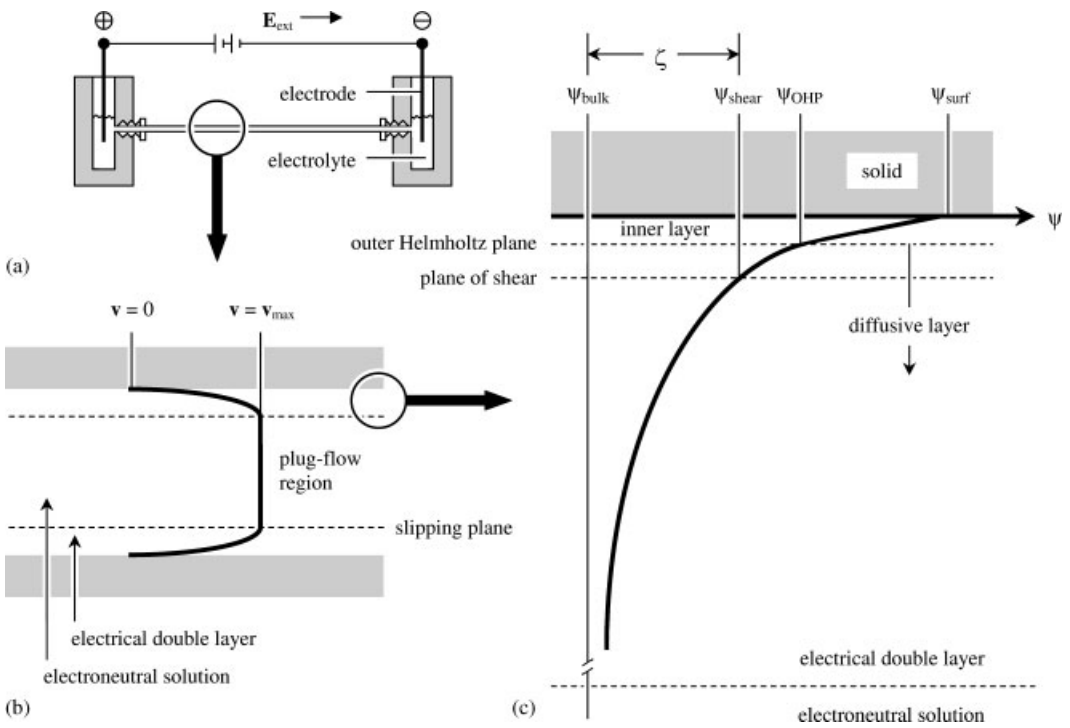

Figure 1. Illustration of electrokinetically driven flow (electroosmosis) through a straight cylindrical capillary with $\zeta < 0$: (a) Experimental set-up; (b) pore-scale velocity profile of electroosmotic flow (EOF); and (c) distribution of electrical potential in the electrical double layer (EDL).

accumulation in this region can be described by the Boltzmann equation. The spatial dimension of the diffusive layer is typically between a few and hundred nanometers.

EOF sets in when an external electrical field ($\mathbf{E}_{\text{ext}} = -\nabla\phi$) is applied. It interacts with the EDL field to create an electrokinetic body force on the liquid. Consequently, the bulk of liquid is driven by viscous drag via the shear stresses concentrated in the relatively thin EDL (compared to a capillary radius r_c of micrometer dimension). The potential (ψ) at the so-called shear plane separating mobile and immobile phases is the electrokinetic or zeta-potential (ζ). For the case considered here (smooth surface, simple ions) ζ should be close to, if not coincident with the diffusive double layer potential ψ_{OHP} (Figure 1(c)). The fluid velocity rises from zero at the shear plane to a limiting value $\mathbf{v}_{\max}$ beyond the EDL where, from a macroscopic point of view, the liquid seems to slip past the surface (Figure 1(b))

$$\mathbf{v}_{\max} = \mu_{\text{eo}}\mathbf{E}_{\text{ext}} = -\varepsilon_0\varepsilon_r\left(\frac{\zeta}{\eta_f}\right)\mathbf{E}_{\text{ext}} \tag{1}$$

μ_{eo} denotes the electroosmotic mobility and η_f is the dynamic viscosity of the fluid. ε_0 is the permittivity of vacuum and ε_r the relative permittivity of the electrolyte solution. The minus sign in Equation (1) means that $\mathbf{v}_{\max}$ and $\mathbf{E}_{\text{ext}}$ are in the same direction when ζ is negative. Without any externally applied pressure forces and uniform distribution of ζ along the channel wall the liquid moves as in plug-flow as the gradient in ψ beyond the EDL is negligible. The thickness of the EDL is characterized by

$$\lambda_D = \left(\frac{\varepsilon_0\varepsilon_r RT}{F^2\sum_i z_i^2 c_{i,\infty}}\right)^{1/2} \tag{2}$$

where R is the gas constant, T the absolute temperature and F Faraday's constant, z_i is the valency of ionic species i and $c_{i,\infty}$ its molar concentration in the electroneutral solution. λ_D is the Debye screening length and about 10 nm for a 10^{-3} M 1:1 aqueous electrolyte solution. In this case the EDL is much smaller than the radius of micrometer channels ($r_c/\lambda_D > 100$) and the volumetric EOF rate is approximately given by $Q = v_{\max}A$ (where A is the cross-sectional area of a channel). However, as the channel diameter approaches submicrometer dimension and/or as λ_D increases the EDL cannot be considered as thin any longer (e.g. $r_c/\lambda_D \approx 10$) and the plug-like velocity profile deteriorates towards a parabola, as known for Poiseuille flow ($r_c/\lambda_D = 2$), with an accompanying increase in hydrodynamic dispersion evidenced by Figure 2 [10, 61].

2.2. General mathematical formulation

The velocity field of an incompressible Newtonian electrolyte solution in low-Reynolds number flow through a microfluidic channel is governed by the Navier–Stokes equation

$$\rho_f\left(\frac{\partial\mathbf{v}}{\partial t} + (\mathbf{v}\cdot\nabla)\mathbf{v}\right) = -\nabla p + \eta_f\nabla^2\mathbf{v} + \mathbf{f} \tag{3}$$

where ρ_f is the density of the fluid, $\mathbf{v}$ represents the divergence-free velocity field ($\nabla\cdot\mathbf{v} = 0$), and p denotes hydrostatic pressure. The body force $\mathbf{f}$ is related to the volume density of

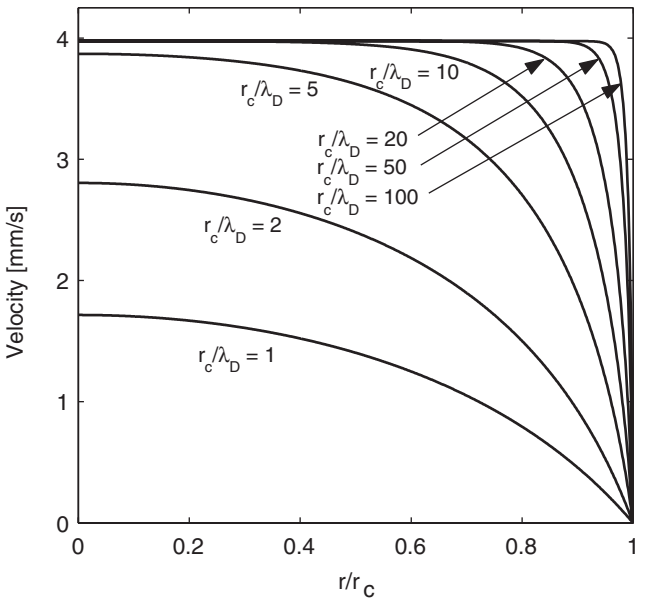

Figure 2. Velocity profiles of EOF in an open-straight, cylindrical capillary for different values of r_c/λ_D obtained by solution of the momentum balance equation [61]. Externally applied electrical field $E_{ext} = 5 \times 10^4\,\mathrm{Vm}^{-1}$, $\zeta = -0.1\,\mathrm{V}$, $\varepsilon_r = 80$; liquid density and viscosity are $10^6\,\mathrm{gm}^{-3}$ and $0.89\,\mathrm{gm}^{-1}\,\mathrm{s}^{-1}$, respectively (at $T = 298.15\,\mathrm{K}$). The Debye screening length (λ_D) is 10 nm.

charge ρ_q and the local electrical field ($\mathbf{E} = -\nabla\Phi$) by

$$\mathbf{f} = \rho_q \mathbf{E} = -q_e \nabla\Phi \sum_{i=1}^{N} z_i n_i \quad \text{for } i = 1, \ldots, N \tag{4}$$

where q_e stands for the elementary charge, n_i is the number concentration of ionic species i in the N-component electrolyte solution, and Φ denotes the local electrostatic potential governed by the Poisson equation

$$\nabla^2\Phi = -\frac{\rho_q}{\varepsilon_0 \varepsilon_r} \tag{5}$$

The flux density $\mathbf{j}_i$ (the number of ions per unit area passing through the surface of a volume element) is related to the local fluid velocity and gradients in ion density and electrical potential by the Nernst–Planck equation

$$\mathbf{j}_i = \left(\mathbf{v} - \frac{q_e z_i D_i \nabla\Phi}{k_B T} \right) n_i - D_i \nabla n_i \tag{6}$$

where D_i is the mass diffusion coefficient and k_B is the Boltzmann constant. Each ionic species satisfies the following conservation:

$$\frac{\partial n_i}{\partial t} + \nabla \cdot \mathbf{j}_i = 0 \tag{7}$$

Together with appropriate initial and boundary conditions Equations (3)–(7) describe the mass transport in systems with arbitrary geometry, distribution (and magnitude) of ζ, and aspect ratio. It is important to note that we consider here (cf. Equations (4)–(6)), without further simplification, the local electrostatic potential in the channel which, in general, includes contributions from both the EDL and $\mathbf{E}_{\text{ext}}$. Further, the presented description does not rely on the Boltzmann distribution for electrical charges in the diffusive part of the EDL applicable only at thermodynamic equilibrium. It would assume that this distribution remains undisturbed by external convective influences which is justified only under certain limiting conditions, e.g. at low Peclet number in channels of arbitrary geometry and for a uniform distribution of ζ [13].

In this work we consider fully developed, steady, isothermal EOF in the microfluidic channel. It eliminates time derivatives in Equations (3) and (7), as well as the need for initial conditions. Thus, we remain concerned with the following set of coupled equations:

$$\rho_{\text{f}}(\mathbf{v}\cdot\nabla)\mathbf{v}=-\nabla p+\eta_{\text{f}}\nabla^2\mathbf{v}-q_{\text{e}}\nabla\Phi\sum_{i=1}^{N}z_i n_i \tag{8a}$$

$$\nabla\cdot\mathbf{v}=0 \tag{8b}$$

$$\nabla^2\Phi=-q_{\text{e}}\sum_{i=1}^{N}z_i n_i/\varepsilon_0\varepsilon_{\text{r}} \tag{8c}$$

$$\mathbf{v}\nabla n_i-D_i\nabla^2 n_i-\frac{q_{\text{e}}z_i D_i}{k_{\text{B}}T}\nabla\cdot(n_i\nabla\Phi)=0 \tag{8d}$$

2.3. Boundary conditions

Because the length of a microfluidic channel is large compared to heterogeneities in the flow field and species transport on any length (and associated time) scale we assume longitudinal spatial periodicity [62]. Consequently, our description reduces to that of a representative unit (Figure 3(a)) with periodic (outer) boundary conditions

$$[|\Phi|]=C,\qquad [|n_i|]=0,\qquad [|\mathbf{v}|]=0 \tag{9}$$

where C is a constant related to the conditions of an experiment (including pH, the electrolyte concentration, $\mathbf{E}_{\text{ext}}$, surface adsorption, or temperature) and $[|\ldots|]$ denotes the difference between values of a function at opposite points lying on the corresponding unit boundaries.

The outer boundary conditions have to be complemented by inner boundary conditions which define the values of the electrical potential (or charge), flow velocity and species number concentrations at the solid–liquid interface. The common no-slip and normal-zero-flux conditions are recognized at this interface for the fluid flow velocity and number concentrations, respectively

$$\mathbf{v}=0 \tag{10a}$$

$$v\cdot\mathbf{j}_i=0 \tag{10b}$$

where v is the outer normal to the solid–liquid interface. In turn, an electrical boundary condition can be represented by either the surface charge density or zeta-potential. Since these characteristics, in particular, depend on both the nature of contacting media and the local

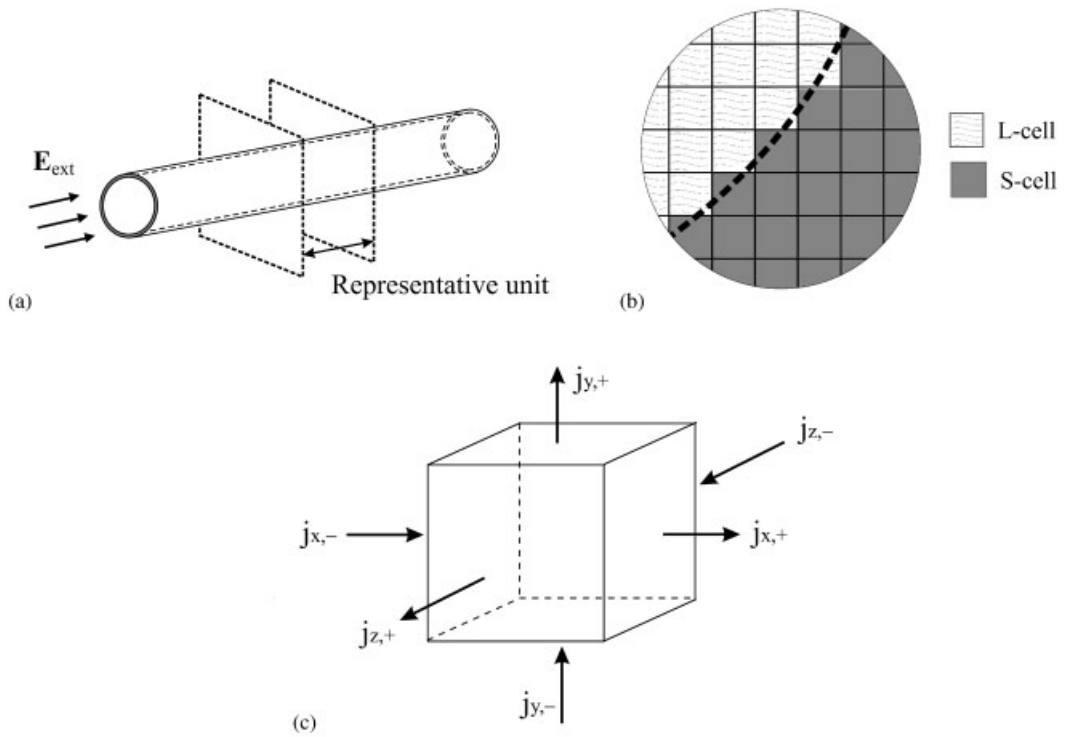

Figure 3. Discretization and approximation of the solution domain: (a) Capillary scale. Spatial periodicity reduces the description to that of a representative unit with periodic boundary conditions; (b) Solid–liquid interface. The solution domain is represented by a set of uniform cubic cells; and (c) Single L-cell. Entry and exit flux density components.

environment, e.g. the interfacial space morphology or the local pH, they can be considered, in general, as spatially variable quantities. Thus, the electrical boundary conditions at the solid–liquid interface can be imposed in two alternative ways: by given surface charge density (σ) or zeta-potential (ζ) distribution, respectively

$$v \cdot \nabla \Phi = -\frac{\sigma(\mathbf{r})}{\varepsilon_0 \varepsilon_r} \tag{11a}$$

or

$$\Phi = \zeta(\mathbf{r}) \tag{11b}$$

The former equation corresponds to the Neumann-type, the latter to the Dirichlet-type boundary condition.

This presentation of inner boundary conditions assumes that the boundary values of all quantities (flow velocity, species flux, surface charge density, zeta-potential) are related to the same location. In fact, while the no-slip and normal-zero-flux conditions, as well as the surface charge density are recognized directly at a solid–liquid interface, the zeta-potential is defined with respect to the shear plane (Figure 1(c)). However, since this plane is located in

immediate proximity ($\approx 0.5\,\mathrm{nm}$) to the solid–liquid interface, it is assumed that these surfaces coincide.

3. COMPUTATIONAL METHODS

3.1. General scheme

To solve the system of time-independent partial differential equations (Equations (8a)–(8d)) subject to inner and outer boundary conditions (Equations (9)–(11)) we implemented an iterative scheme (Figure 4). At each iteration first the coupled Nernst–Planck and Poisson equations (Equations (8c) and (8d)) were solved numerically. Then, the Navier–Stokes equation (Equation (8a)) together with the continuity equation (Equation (8b)) were solved. The iterative solution had continued until convergence of the flow field was reached. As initial guess we used zero flow field, as well as bulk number concentrations and the electrical potential distribution caused by the applied field. This contribution to the local electrical potential is assumed to be point-wise constant during iterations.

Thus, the numerical scheme requires solution of Poisson, Nernst–Planck, and Navier–Stokes equations (where the last problem is, by far, the more difficult computational task). While

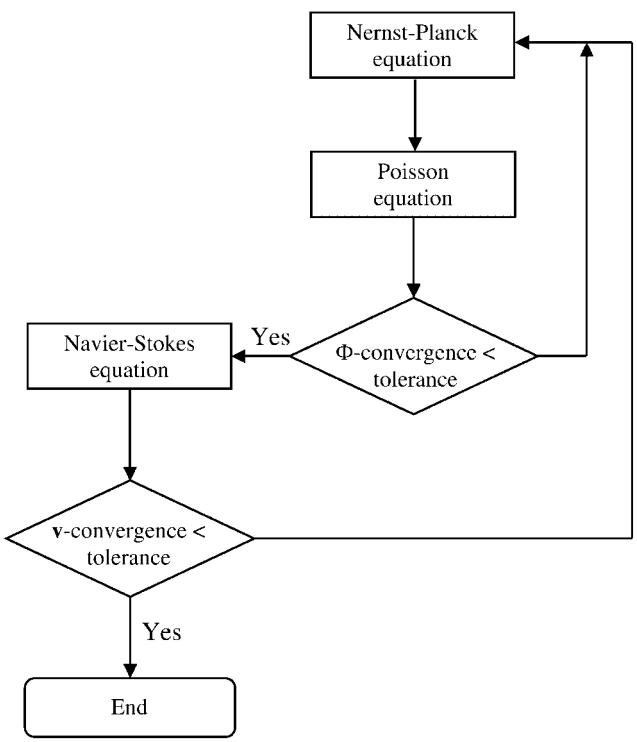

Figure 4. Flow-chart of the computational scheme employed for the PNP–LB (Poisson–Nernst–Planck coupled with lattice-Boltzmann) simulations.

we employed traditional finite-difference methods to resolve the first two problems, the lattice-Boltzmann method has been applied for solution of the Navier–Stokes problem.

3.2. Geometry and discretization of the solution domain

A uniform mesh has been utilized for numerical solution of all of the above-mentioned problems. Thus, the solution domain can be represented by a set of equal cubic cells of size h (Figure 3(b)). Cells were divided into two subsets, i.e. cells having their geometrical centre in the liquid phase (L-cells) or in the solid phase (S-cells). During a simulation the electrical potential, charge number concentration, and fluid velocity are determined at the centres of only the L-cells. S-cells adjacent to L-cells are considered as interface cells and the actual values of physical quantities at their centres are used as boundary values.

3.3. Numerical solution of the Poisson–Nernst–Planck problem

The finite-difference scheme for solution of the Nernst–Planck equation is based on the total flux density in an L-cell. For steady-state the net flux is zero. This situation can be represented by entry and exit components on each of the six cell surfaces (Figure 3(c))

$$j^{x,+}_{k,l,m} + j^{x,-}_{k,l,m} + j^{y,+}_{k,l,m} + j^{y,-}_{k,l,m} + j^{z,+}_{k,l,m} + j^{z,-}_{k,l,m} = 0 \tag{12}$$

where k, l, and m define the discrete co-ordinates of a cell. If an L-cell is not lying adjacent to the interface each of the flux density components is expressed in terms of the flow velocity, concentration, and electrical potential at the centre of a given and neighbouring points. For a particular species, for example, we have

$$j^{x,+}_{k,l,m} = \frac{v^x_{k+1,l,m} + v^x_{k,l,m}}{2}\frac{n_{k+1,l,m} + n_{k,l,m}}{2} - D\frac{n_{k+1,l,m} - n_{k,l,m}}{h} - \frac{q_e z D}{k_B T}\frac{n_{k+1,l,m} + n_{k,l,m}}{2}\frac{\Phi_{k+1,l,m} - \Phi_{k,l,m}}{h} \tag{13}$$

If an L-cell is adjacent to the interface and the normal-zero-flux boundary condition is applied, the corresponding term in Equation (12) is eliminated. By assuming that interface and boundary values lie on the border between L- and S-cells the distance $h/2$ (instead of h) should be used. This is consistent with the location of the no-slip wall in LB simulations based on the bounce-back boundary condition [63]. By using similar expressions for the other flux components, substituting into Equation (12), and solving the equation for $n_{k,l,m}$ one can obtain an explicit expression for calculation of its updated value. It is determined by the concentration values from a previous iteration, as well as with the flow velocity and electrical potential values in a given and neighbouring cells. We used an SOR scheme to get a more rapid convergence

$$\hat{n}_{k,l,m} = \omega n_{k,l,m} + (1-\omega)\check{n}_{k,l,m} \tag{14}$$

where $\hat{n}_{k,l,m}$ is updated number concentration at current iteration, $\check{n}_{k,l,m}$ is the number concentration from previous iteration, and ω is the relaxation parameter. Then, updated number concentration values for each species in all cells are used for solution of the Poisson equation.

Its finite-difference representation is

$$-\frac{\sum n_{k,l,m} z q_e}{\varepsilon_0 \varepsilon_r} = \frac{2}{h_{k+1/2}+h_{k-1/2}}\left(\frac{\Phi_{k+1,l,m}-\Phi_{k,l,m}}{h_{k+1/2}} - \frac{\Phi_{k,l,m}-\Phi_{k-1,l,m}}{h_{k-1/2}}\right) + \frac{2}{h_{l+1/2}+h_{l-1/2}}\left(\frac{\Phi_{k,l+1,m}-\Phi_{k,l,m}}{h_{l+1/2}} - \frac{\Phi_{k,l,m}-\Phi_{k,l-1,m}}{h_{l-1/2}}\right) + \frac{2}{h_{m+1/2}+h_{m-1/2}}\left(\frac{\Phi_{k,l,m+1}-\Phi_{k,l,m}}{h_{m+1/2}} - \frac{\Phi_{k,l,m}-\Phi_{k,l,m-1}}{h_{m-1/2}}\right) \tag{15}$$

where, for example, $h_{k+1/2}$ is the distance between the centres of cells $(k+1,l,m)$ and (k,l,m); the summation should be made over all ionic species. As for the Nernst–Planck equation, this expression needs to be modified if the cell is adjacent to the interface, by replacing either the corresponding distance h by $h/2$ (Dirichlet boundary condition) or the corresponding potential difference by $2\sigma/(h\varepsilon_0\varepsilon_r)$ (Neumann boundary condition). By applying the traditional Gauss–Seidel iterative procedure Equation (15) allows to obtain an explicit expression for determination of the updated value of electrical potential which, in the case of the Dirichlet boundary condition, can be written as,

$$\hat{\Phi}_{k,l,m} = \left(\frac{1}{h_{k+1/2}h_{k-1/2}} + \frac{1}{h_{l+1/2}h_{l-1/2}} + \frac{1}{h_{m+1/2}h_{m-1/2}}\right)^{-1} \times \left(\frac{\sum n_{k,l,m} z q_e}{2\varepsilon_0\varepsilon_r} + \frac{h_{k-1/2}\check{\Phi}_{k+1,l,m} + h_{k+1/2}\,\hat{\Phi}_{k-1,l,m}}{h_{k+1/2}h_{k-1/2}(h_{k+1/2}+h_{k-1/2})} + \frac{h_{l-1/2}\check{\Phi}_{k,l+1,m} + h_{l+1/2}\,\hat{\Phi}_{k,l-1,m}}{h_{l+1/2}h_{l-1/2}(h_{l+1/2}+h_{l-1/2})} + \frac{h_{m-1/2}\check{\Phi}_{k,l,m+1} + h_{m+1/2}\,\hat{\Phi}_{k,l,m-1}}{h_{m+1/2}h_{m-1/2}(h_{m+1/2}+h_{m-1/2})}\right) \tag{16}$$

The calculations of the number concentration and electrical potential stop when the convergence rate

$$\chi_{PNP} = \sqrt{\frac{\sum_{k,l,m}(\hat{\Phi}_{k,l,m} - \check{\Phi}_{k,l,m})^2}{\sum_{k,l,m}\check{\Phi}^2_{k,l,m}}} \tag{17}$$

becomes less than the predefined value δ_{PNP} (PNP $\equiv$ Poisson–Nernst–Planck), which is typically set to 10^{-6}.

3.4. The lattice-Boltzmann algorithm

The electrolyte solution as a statistical system can be described in terms of a distribution function $\mathscr{F}(\mathbf{r},\mathbf{u},t)$ defined such that $\mathscr{F}(\mathbf{r},\mathbf{u},t)\,d\mathbf{r}\,d\mathbf{u}$ gives the number of fluid molecules which, at time t, are located between $\mathbf{r}$ and $(\mathbf{r}+d\mathbf{r})$ and have velocities in a range from $\mathbf{u}$ to $(\mathbf{u}+d\mathbf{u})$.

Macroscopic quantities like the fluid density ρ_f and the velocity $\mathbf{v}$ can be determined by momentum integration of this distribution function

$$\rho_f(\mathbf{r},t) = \int M_m \mathscr{F}(\mathbf{r},\mathbf{u},t)\,d\mathbf{u} \tag{18}$$

and

$$\mathbf{v}(\mathbf{r},t) = \frac{1}{\rho_f(\mathbf{r},t)} \int M_m \mathbf{u} \mathscr{F}(\mathbf{r},\mathbf{u},t)\,d\mathbf{u} \tag{19}$$

where M_m denotes molecular mass. The evolution of the distribution function can be described by the following equation:

$$\mathscr{F}\left(\mathbf{r}+\mathbf{u}\,dt, \mathbf{u}+\frac{\mathbf{F}}{M_m}dt, t+dt\right) d\mathbf{r}\,d\mathbf{u} = \mathscr{F}(\mathbf{r},\mathbf{u},t) + \Omega(\mathscr{F})\,d\mathbf{r}\,d\mathbf{u}\,dt \tag{20}$$

where $\mathbf{F}$ is the acting external force and Ω denotes the collision operator. It is well known that the macroscopic properties are not directly dependent on the details of the microscopic behaviour, but are mainly defined through interactions between molecules expressed, for example, by an appropriate collision operator. Thus, the transition toward a simplified dynamics with discrete space, time and molecular velocities is feasible. The discrete analogy of Equation (20) is

$$\mathscr{F}_\alpha(\mathbf{r}+\mathbf{e}_\alpha \Delta t, t+\Delta t) = \mathscr{F}_\alpha(\mathbf{r},t) + \Omega_\alpha(\mathscr{F}_\alpha) + \Delta t F_\alpha \tag{21}$$

where $\mathscr{F}_\alpha$ is the distribution function for the αth discrete velocity $\mathbf{e}_\alpha$ at position $\mathbf{r}$ and time t, and Δt is the time step. In this work we are concerned with a modification of the LB approach, the so-called lattice-BGK (Bhatnagar–Gross–Krook) model [34, 52], being characterized by the discrete Boltzmann equation with a single-time relaxation collision operator

$$\mathscr{F}_\alpha(\mathbf{r}+\mathbf{e}_\alpha \Delta t, t+\Delta t) = \mathscr{F}_\alpha(\mathbf{r},t) + \frac{1}{\tau}[\mathscr{F}_\alpha^{eq}(\mathbf{r},t) - \mathscr{F}_\alpha(\mathbf{r},t) + \Delta t F_\alpha] \tag{22}$$

where $\mathscr{F}_\alpha^{eq}$ represents the equilibrium distribution function and τ is a non-dimensional relaxation time. For the D_3Q_{19} lattice-BGK model [32] $\mathscr{F}_\alpha^{eq}$ can be expressed by,

$$\mathscr{F}_\alpha^{eq} = \rho_f w_\alpha \left[1 + \frac{3}{c_s^2}\mathbf{e}_\alpha \cdot \mathbf{v} + \frac{9}{2c_s^4}(\mathbf{e}_\alpha \cdot \mathbf{v})^2 - \frac{3}{2c_s^2}\mathbf{v}\cdot\mathbf{v}\right] \tag{23}$$

where c_s is the speed of sound and w_α is a weighting factor depending on the length of the vector $\mathbf{e}_\alpha$ given by [52]

$$w_\alpha = \begin{cases} 1/3, & \alpha = 0 \text{ (rest particle)} \\ 1/18, & \alpha = 1,2,\ldots,6 \text{ (nearest neighbours)} \\ 1/36, & \alpha = 7,8,\ldots,18 \text{ (next-nearest neighbours)} \end{cases} \tag{24}$$

Incorporation of a body force term caused by the interaction of the EDL field with the externally applied electrical field into the discrete Boltzmann equation was performed using

the method described by Guo *et al.* [64]

$$F_\alpha = \left(1 - \frac{1}{2\tau}\right) w_\alpha \left[\frac{\mathbf{e}_\alpha - \mathbf{v}}{c_s^2} + \frac{(\mathbf{e}_\alpha \cdot \mathbf{v})}{c_s^4}\mathbf{e}_\alpha\right] \cdot \mathbf{F} \tag{25}$$

To satisfy the no-slip boundary condition for velocity at the solid–liquid interface, we employed the conventional bounce-back scheme, where momentum from an incoming particle is bounced back in opposite direction when it hits the wall.

After each iteration the divergence rate

$$\chi_{NS} = \sqrt{\frac{\sum_{k,l,m}(\hat{\mathbf{v}}_{k,l,m} - \check{\mathbf{v}}_{k,l,m})^2}{\sum_{k,l,m}\check{\mathbf{v}}_{k,l,m}^2}} \tag{26}$$

is calculated and compared with a predefined value of δ_{NS} (NS $\equiv$ Navier–Stokes). The simulation stops when $\chi_{NS} < \delta_{NS}$ (typically 10^{-4}) is satisfied.

Here, it should be noted that the overwhelming majority of real electrokinetic systems operates in the low-Mach number limit which is a necessary condition for application of the LB method. Typical EOF velocities are of the order of a few millimeters per second which is much less than the speed of sound in liquid media.

4. RESULTS OF SIMULATIONS

4.1. Homogeneous equilibrium double layer

Although the presented model is capable of dealing with both arbitrary distribution of ζ and geometrical configuration of the solid–liquid interface, we started to simulate EOF in relatively simple systems for which either an analytical solution to the problem exists or the results of other numerical simulations are available for comparison. Quantitative analysis of computed fields of a physical quantity Θ (e.g. species number concentration or flow velocity components) is based on the global relative error γ defined with respect to some appropriate reference value

$$\gamma = \frac{\sqrt{\sum(\Theta - \Theta_{ref})^2}}{\sqrt{\sum \Theta_{ref}^2}} \tag{27}$$

In particular, for the lattice-Boltzmann EOF velocity field in a homogeneous capillary the reference values may be obtained by numerical solution of the momentum balance equation using the Runge–Kutta method.

To test the adequacy of the model for simulating electrical charge distributions in the diffusive part of the EDL (cf. Figure 1(c)) we begin with an isolated, homogeneous solid–liquid interface for which the typical dimension of surface roughness is smaller than the EDL thickness, and simulate the ionic number concentration in the electrolyte in contact with this surface by solving the Poisson and Nernst–Planck problems. At equilibrium, without concentration gradients and any externally applied field, the electrical potential distribution can be

obtained from the Poisson–Boltzmann equation

$$\nabla^2\psi = -\frac{q_e}{\varepsilon_0\varepsilon_r}\sum_{i=1}^{N} z_i n_{i,\infty}\exp\left(-\frac{q_e z_i \psi}{k_B T}\right) \tag{28}$$

where the local concentration is determined by the Boltzmann distribution

$$n_i = n_{i,\infty}\exp\left(-\frac{q_e z_i \psi}{k_B T}\right) \tag{29}$$

The analytical solution of Equation (28) (the starting point of the Gouy–Chapman description [65] of the diffusive EDL) for a charged, flat surface, a symmetrical 1:1 electrolyte such as NaCl ($z_1 = -z_2 = z$), and an arbitrary magnitude, but uniform distribution of the zeta-potential (ζ) is [66]

$$\psi(x) = \frac{2k_B T}{q_e z}\ln\left[\frac{1 + e^{-x/\lambda_D}\tanh\left(\frac{q_e z\zeta}{4k_B T}\right)}{1 - e^{-x/\lambda_D}\tanh\left(\frac{q_e z\zeta}{4k_B T}\right)}\right] \tag{30}$$

where x is the distance from the surface. For values of ζ low enough (below ca. 25 mV) Equation (30) reduces to the so-called Debye–Hückel equation, $\psi(x) = \zeta e^{-x/\lambda_D}$. Results for the distribution of net electrical charge density based on the analytical solution (Equations (29) and (30)) and the numerical treatment outlined in Section 3.3 are shown in Figure 5. Because λ_D appears as characteristic decay length for the potential, we analysed the global relative error in dependence of the grid resolution with respect to λ_D (see inset). As electrolyte we considered an aqueous solution of NaCl at 298.15 K with concentration (9.43×10^{-4} M) adjusted

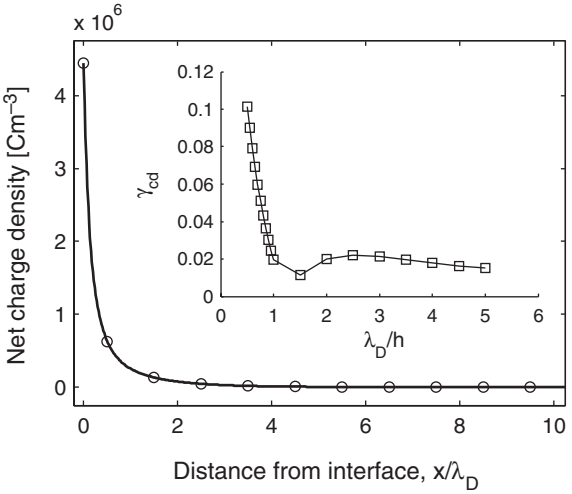

Figure 5. Distribution of net electrical charge in the EDL at a flat solid–liquid interface (the open circles are the results of the numerical solution, solid line: analytical solution) and dependence of the global relative error (γ_{cd}) on the grid resolution with respect to the double layer thickness (inset).

such that λ_D is 10 nm (Equation (2)), while the surface is characterized by $\zeta = -100$ mV. One conclusion to be drawn from Figure 5 is that the net charge density (cd) away from a charged surface can be computed with global relative errors (γ_{cd}) better than 2% for a grid resolution λ_D/h of 1 and higher ($\gamma_{cd} = 0.59\%$ for $\lambda_D/h = 30$) by using the Poisson–Nernst–Planck solver described above (in Section 3.3). It is further evident that after a distance of about $5\lambda_D$ from the surface the solution is practically electroneutral. Recalling that this distance is about 50 nm under the present set of conditions, it is only a thin liquid layer close to the interface that becomes locally charged, in general, when considering electrolytes confined by pores of micrometer dimension.

4.2. Straight, homogeneous cylindrical capillary

As a next step, we simulated EOF in a straight, homogeneous cylindrical capillary. The spatial homogeneity of this system alleviates the use of an iterative procedure for obtaining the steady-state velocity field. Ionic number concentrations are not disturbed by forced convection. Thus, the Poisson–Nernst–Planck solver and LB-code are run only once. Because there is no general analytical solution available for the EOF problem in a cylindrical capillary, the simulated velocity field was compared with one obtained by numerical solution of the one-dimensional momentum balance equation [61]

$$\frac{d^2 v_x}{dr^2} + \frac{1}{r}\frac{dv_x}{dr} = \frac{2E_{ext} q_e n_\infty}{\eta_f} \sinh\left(\frac{q_e \psi}{k_B T}\right) \tag{31}$$

The solution of this equation provides the radial distribution of axial EOF velocities in the cylindrical capillary. Equation (31) was solved with a very fine resolution (2×10^5 points per channel diameter). Further, the use of different capillary radii allowed to realize aspect ratios r_c/λ_D from 10 to 100. Figure 6 compares velocity profiles obtained by both procedures. As was already emanating from Figure 5, an applied electrical field will be interacting with the electrolyte solution only in the EDL where the liquid has acquired a net charge. Thus, the driving force for EOF is not constant over the capillary diameter: it dominates in vicinity of the capillary wall, but soon becomes zero in the central region of the capillary lumen. There, motion of bulk liquid is caused by a viscous drag force leading to the plug-like velocity distribution beyond the slipping plane (Figure 1(b)). The dependence of the global relative error γ_{vf} of the axial component in a velocity field (vf) on the spatial resolution with respect to the capillary radius is demonstrated in Figure 7 for various aspect ratios. It should be mentioned that the error associated with the spatial resolution manifests itself in an inaccuracy of both the calculated electrical charge distribution (which, in turn, is affected by the simulated electrical potential distribution) and velocity field. This can explain why the total error γ_{vf} does not exhibit the squared dependence on grid resolution which is inherent individually in the finite-difference and LB methods. Nevertheless, one can achieve higher accuracy by grid refinement, e.g. the use of 100 grid points over a capillary radius r_c resulted in γ_{vf} of less than 6% (for all aspect ratios). On the other hand, the computational time grows with the third power of the spatial resolution.

The complete simulation of EOF in a cylindrical capillary (for $r_c/h = 50$) took about 15 CPU minutes per cross-sectional layer for one computer node. In general, simulations were performed on a Hewlett-Packard Superdome at the Otto-von-Guericke-Universität Magdeburg, Germany.

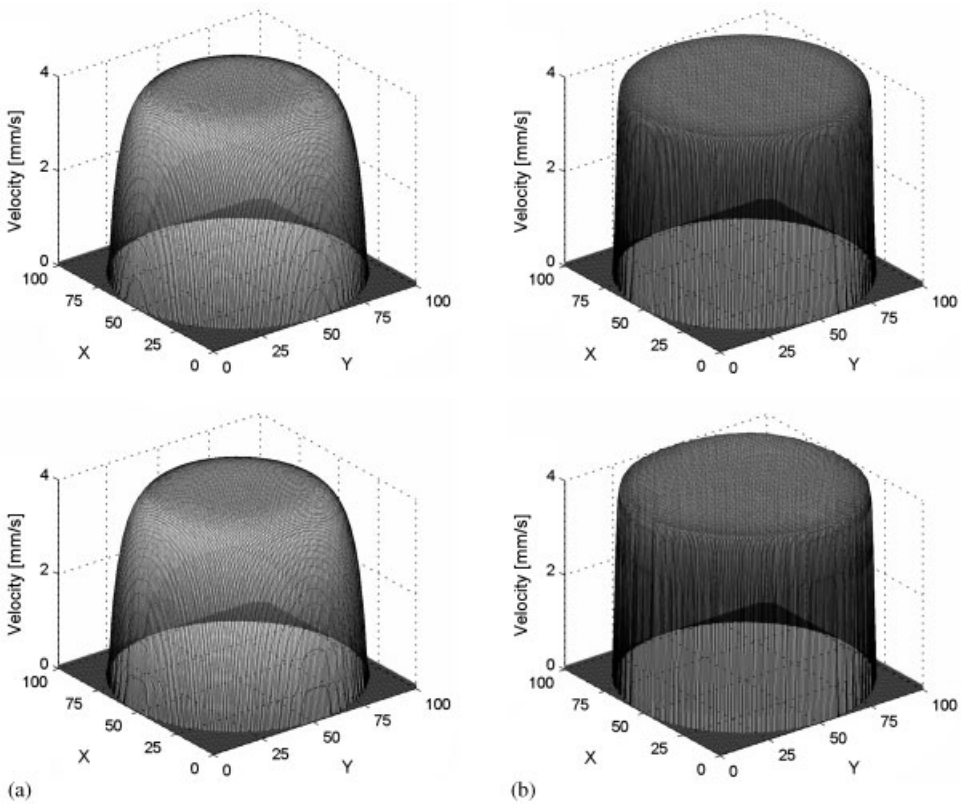

Figure 6. EOF velocity field in an open-straight, cylindrical capillary with homogeneous and smooth surface: solution of the momentum balance equation (top) vs the PNP–LB approach (bottom) for: (a) $r_c/\lambda_D = 10$; and (b) $r_c/\lambda_D = 100$. The same conditions as in Figure 2 have been used.

4.3. Straight cylindrical capillaries with axial and angular inhomogeneities in electrokinetic potential

Then, we modelled EOF in cylindrical capillaries with a destinated axial and angular distribution of the zeta-potential (Figure 8). This configuration can be considered as simplified approach for dealing with a heterogeneous surface charge distribution in porous media under more general conditions. In fact, the spatial scale of locally varying electrical potential is often significant with respect to the thickness of the EDL, and it can have a number of reasons. For example, it can already be introduced by the inherent manufacturing process of a material, specific ageing, the storage conditions, chemical reactions, or the eventually irreversible adsorption of molecular or colloidal species on the surface, with a concomitant change of local roughness and electrokinetic properties [61, 67–73]. Consequently, the favourable, i.e. plug-like EOF velocity profile becomes disturbed by induced pressure gradients resulting from an axial variation of the surface charge at the inner wall of a microfluidic channel [71–74]. In turn, this necessarily leads to additional hydrodynamic dispersion. The problem becomes especially severe for the transport of sample mixtures containing large biomolecules such as

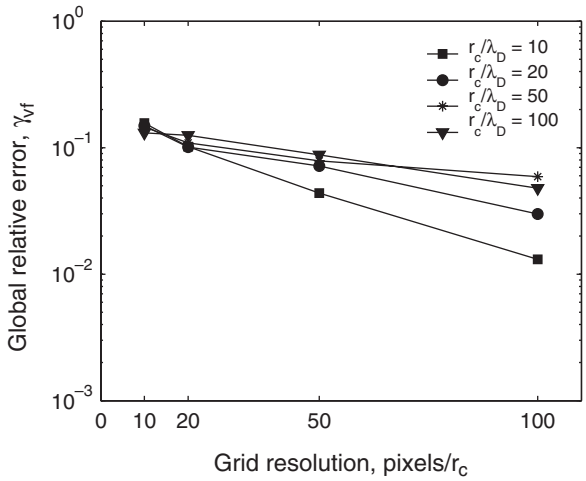

Figure 7. Global relative error of a simulated velocity field (γ_{vf}) relative to the solution of the momentum balance equation: accuracy of the followed PNP–LB approach depending on the spatial resolution with respect to a capillary radius at various aspect ratios (r_c/λ_D).

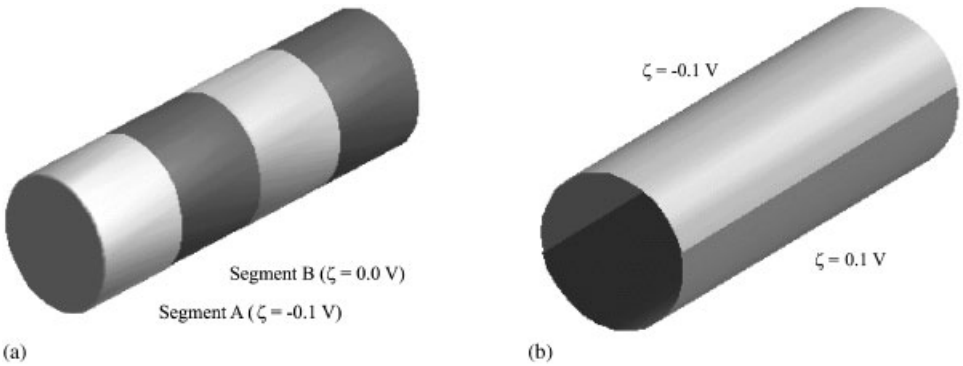

Figure 8. Inhomogeneous charge distributions (discrete patterns) at the inner wall of the cylindrical capillary: (a) Surface charge pattern 1 (P1): Step changes of ζ in the axial direction, angular uniformity; and (b) P2: Step changes of ζ in the angular direction, axial uniformity.

proteins, peptides or DNA [75] which are charged and, thus, can interact strongly with the often oppositely charged surface through hydrophobic and electrostatic mechanisms. As their adsorption progresses in time, it continues to cause unreproducible local, as well as average EOF velocities and a significant loss of resolution in the separation of individual components due to increased axial dispersion and a strong tailing in the residence-time distributions characterized by non-Gaussian shape.

In general, local variations in electrical potential produce a non-uniform electrokinetic driving force that requires local (positive or negative) pore pressure for compensating the associated momentum in an incompressible fluid [71–74]. Unfortunately, the actual spatial and

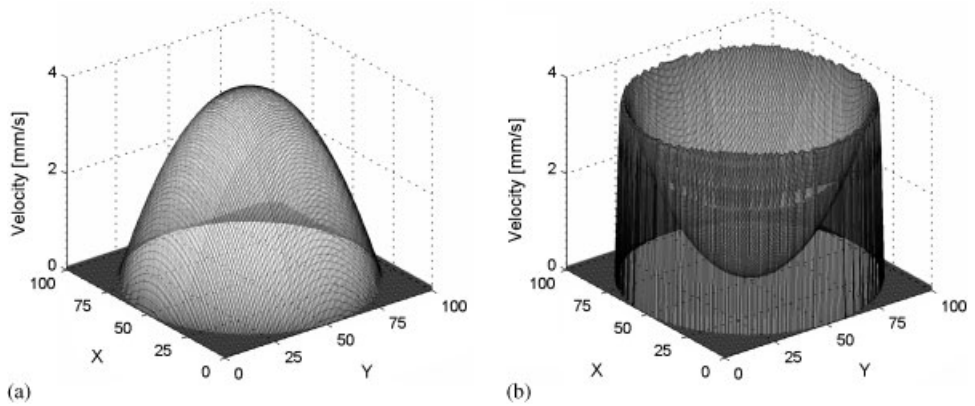

Figure 9. Local flow profiles in the capillary with surface charge pattern P1 (cf. Figure 8(a)). Velocity distributions in the central cross-section of each segment: (a) segment A ($\zeta = -100\,\mathrm{mV}$); and (b) segment B ($\zeta = 0\,\mathrm{mV}$). The Debye screening length (λ_D) is 10 nm and $r_c/\lambda_D = 100$; $E_{ext} = 5 \times 10^4\ \mathrm{V\,m^{-1}}$, liquid density and viscosity are $10^6\ \mathrm{gm^{-3}}$ and $0.89\ \mathrm{gm^{-1}\,s^{-1}}$, respectively, $\varepsilon_r = 80$, $T = 298.15\,\mathrm{K}$.

temporal distribution of electrical potential in a real porous medium usually is unknown making it difficult to study on a quantitative basis. On the other hand, this effect may be tailored, e.g. for enhanced microfluidic mixing, by employing surfaces with a patterned charge distribution [27, 76]. For example, Stroock *et al.* [76] studied EOF driven by two patterned geometries in rectangular microchannels in the limit of a thin EDL. They considered variations of surface charge both parallel and perpendicular to the applied electrical field: While a recirculating flow develops in the former case, multidirectional flow along the field and channel axis results in the latter [76]. Because these types of pattern act as a basis from which more general three-dimensional flows may be constructed and the fluid mechanical consequences of (non)intended surface charge distributions in microfluidic environments be evaluated [77], we treated similar zeta-potential distributions in cylindrical capillaries (Figure 8). The first pattern (P1) consists of cylindrical segments with spatially constant non-zero and zero zeta-potential, alternating in the axial direction and having the length $l = 2r_c$. The second pattern (P2) contains half-cylinders with zeta-potentials of opposite sign, but identical magnitude. The EOF simulations were carried out with a computational resolution of $r_c/h = 100$ ($\lambda_D/h = 2$). Characteristic local velocity distributions for steady, fully-developed flow resulting when an external electrical field is superimposed on the EDL field in a general electrolyte solution in contact with surface patterns P1 and P2 are shown in Figures 9 and 10, respectively.

The EOF in capillaries with heterogeneous distribution of surface charge (or value of ζ) has been the topic of several previous studies. Anderson and Idol [67] have developed an infinite-series analytical solution for EOF through a cylindrical capillary with zeta-potential varying periodically and solely in the axial direction. Using a similar approach Long *et al.* [74] obtained an explicit solution for specific surface charge defects. Herr *et al.* [71] considered the EOF in a cylindrical capillary with step-change in ζ in the axial direction and obtained good agreement with their experimental data. Potoček *et al.* [68] and Ren and Li [61] have numerically studied velocity distributions for EOF in circular microchannels for various non-uniform distributions of ζ. More recently, Gleeson [78] developed an analytical solution for

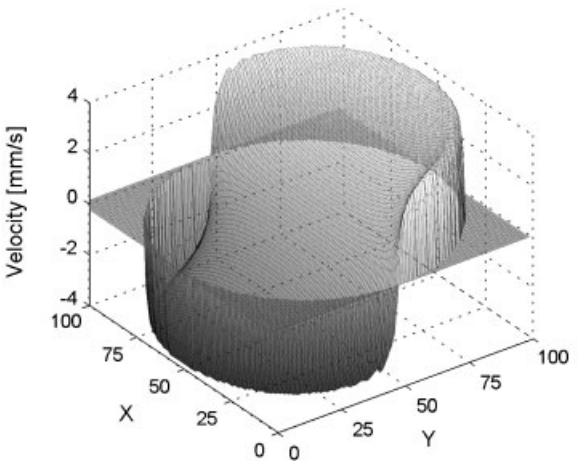

Figure 10. Simulated axial velocity distribution in a cross-section of the open cylindrical capillary with surface charge pattern P2 (cf. Figure 8(b)) for $r_c/\lambda_D = 100$ ($r_c = 1\ \mu m$) and the same conditions as in Figure 9.

the EOF problem in a cylindrical capillary with random zeta-potential distribution. It should be noted that all of the above-mentioned studies were dealing with an axisymmetrical heterogeneity only. Moreover, but except for the work of Ren and Li [61], they assumed a small EDL thickness which allowed to replace the no-slip boundary condition for the velocity at the solid–liquid interface by the Helmholtz–Smoluchowski apparent-slip velocity (Equation (1)) and simplify the analytical solution. Ghosal [72] presented a theory for EOF in channels of arbitrary cross-sectional geometry and distribution of ζ in the lubrication-limit where all axial variations exist on length scales that are large with respect to a characteristic microchannel width, but the assumption of a thin EDL also has been involved in that theory. Thus, reference values for a quantitative analysis of the accuracy with which LB flow fields were computed can be obtained only on the basis of this approximation. It should be pointed out that the slip boundary condition eliminates a fluid region close to the surface where the velocity rises from zero to the bulk value at the slipping plane. Since the thickness of this region does not depend on the channel geometry, the relative contribution of that simplification to the total error decreases with increasing channel diameter (or characteristic transverse dimension).

For a thin EDL the relation between local flow velocity and radial position in capillary segments *A* or *B* of P1 (Figure 8(a)) can be expressed by [71]

$$v_{seg}(r) = -\frac{\varepsilon_0 \varepsilon_r E_{ext}}{\eta_f}\left[\zeta_{seg} + 2(\zeta_{av} - \zeta_{seg})\left(1 - \frac{r^2}{r_c^2}\right)\right] \tag{32}$$

where ζ_{av} is the average value of ζ at the capillary inner wall (for P1 $\zeta_{av} = -50$ mV) and r_c denotes the capillary radius (the subscript 'seg' refers to $\zeta = 0$ mV or $\zeta = -100$ mV, respectively). The velocity profiles calculated by using Equation (32) and compared to those obtained from simulated LB flow fields are shown in Figure 11. The low-velocity region close to the capillary wall in the computed flow field reduces average velocity relative to the value defined by integration of Equation (32) along the radial direction. However, as mentioned

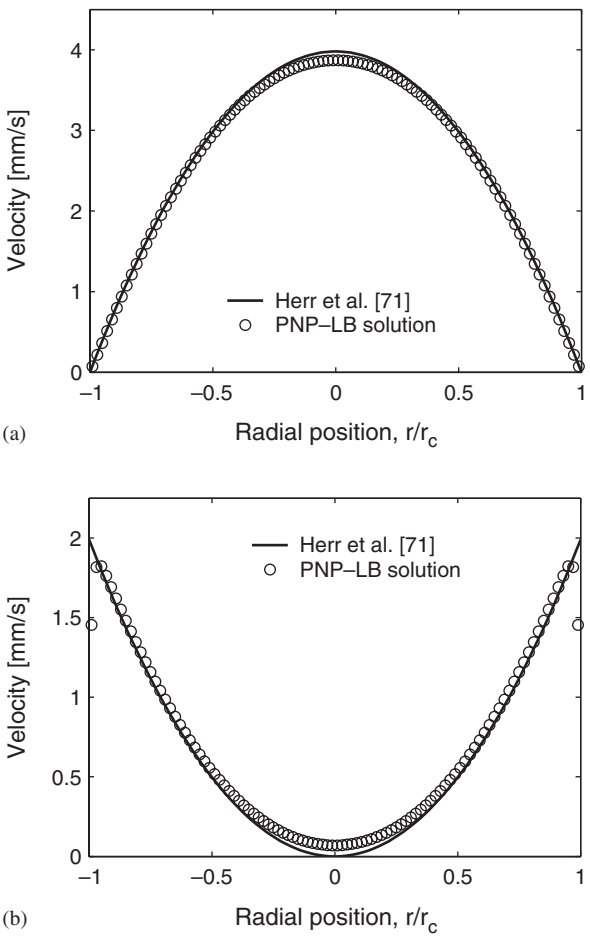

Figure 11. Capillary with pattern P1. Comparison of the simulated intrasegmental velocity profiles with the analytical solution [71]: (a) Central cross-section of segment A ($\zeta = -100$ mV); and (b) central cross-section of segment B ($\zeta = 0$ mV).

above, the discrepancy decreases with an increasing aspect ratio, e.g. the difference between simulated and calculated mean velocities for $r_c/\lambda_D = 100$ is only 0.45%, while it is 9.7% for $r_c/\lambda_D = 20$ and 16.7% for $r_c/\lambda_D = 10$.

In contrast to the discrete axial heterogeneity of P1, the second pattern (Figure 8(b)) is characterized by an azimuthal inhomogeneity. The velocity field for P2 can be obtained in the lubrication limit [72] by numerical solution of the boundary-value problem in polar co-ordinates for an effective potential $\xi(\rho, \theta)$ (ρ and θ are radial and azimuthal co-ordinates)

$$\frac{1}{\rho}\frac{\partial}{\partial\rho}\left(\rho\frac{\partial\xi}{\partial\rho}\right) + \frac{1}{\rho^2}\frac{\partial^2\xi}{\partial\theta^2} = 0, \quad \begin{matrix} \xi(r_c,\theta)|_{0\leqslant\theta<\pi} = -\zeta \\ \xi(r_c,\theta)|_{\pi\leqslant\theta<2\pi} = \zeta \end{matrix} \tag{33}$$

The flow velocity then can be determined from Equation (1) by replacing the local electrical potential ψ by the effective potential ξ, and a solution of this problem (Equation (33)) may be obtained via the following expansion [72]:

$$\xi = -\tilde{\zeta}_0 - \sum_{m=1}^{\infty} [\tilde{\zeta}_m \exp(\mathrm{i}m\theta) + \tilde{\zeta}_m^* \exp(-\mathrm{i}m\theta)]\rho^m \tag{34}$$

where $\tilde{\zeta}_m$ $(m = 0, 1, \ldots, \infty)$ is the complex Fourier transform

$$\tilde{\zeta}_m = \frac{1}{2\pi} \int_0^{2\pi} \zeta(\theta) \exp(-\mathrm{i}m\theta)\, \mathrm{d}\theta \tag{35}$$

It should be pointed out that a quantitative evaluation of the differences between the two discrete velocity fields obtained (i) by numerical solution of this problem (Equations (33)–(35)) and (ii) from computer simulation becomes difficult due to the different co-ordinate systems. While the numerical solution requires the utilization of the polar or, at least, cylindrical system, the PNP–LB computer simulations are realized in the cartesian co-ordinate system. As a result, we have two sets of points corresponding to the polar mesh and rectangular grid.

Therefore, we analysed the two velocity fields by using some of their characteristic properties. It is obvious that, due to the antisymmetry of the zeta-potential distribution in P2 with respect to a centre plane passing through the wall points where the sign of ζ changes, the velocity distribution should possess a similar antisymmetry and any net volumetric flow through the capillary should vanish. Indeed, the simulated velocity field demonstrates such 'self-compensation' (Figure 10) by a deviation of the average velocity from zero of less than 10^{-6}% as compared to the average velocity in the capillary with uniform zeta-potential ($\zeta = -100\,\mathrm{mV}$).

The velocity profiles in the plane $[\theta = \pi/2, 3\pi/2]$, which is perpendicular to the antisymmetry plane, obtained by solution of the problem in Equations (33)–(35) and by computer simulation are shown in Figure 12. Since electromotive forces are effective only in a small region

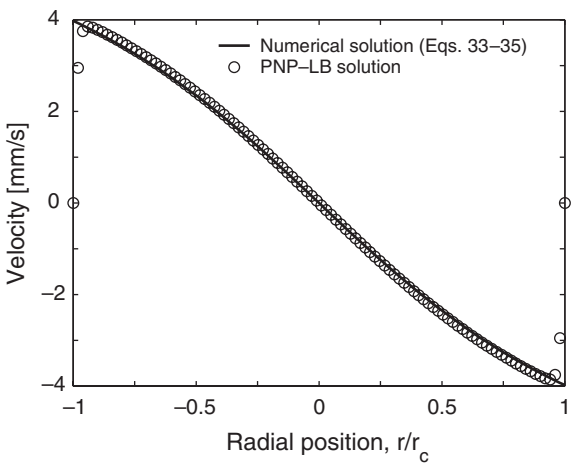

Figure 12. Comparison of velocity distributions in the plane $[\theta = \pi/2, 3\pi/2]$ for the capillary with surface charge pattern P2.

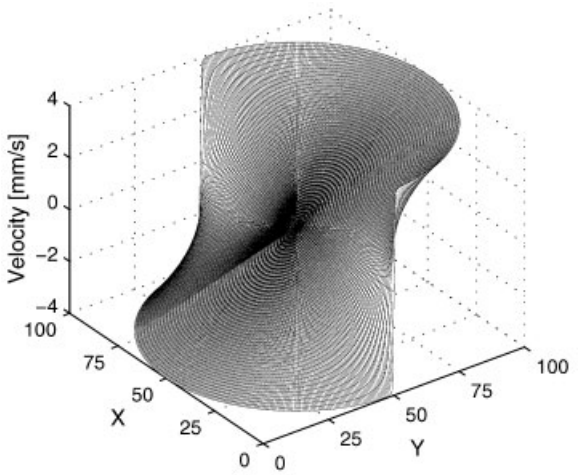

Figure 13. Velocity profile in a cross-section of the open cylindrical capillary ($r_c = 1\ \mu m$) with surface charge pattern P2 according to the approach of Ghosal [72]. The same conditions as in Figures 9 and 10 have been used.

close to the wall of the capillary, actual differences in the velocity profiles should be explainable by the respective velocity boundary conditions. While the slip-condition assumes a discontinuous change of velocity at points where ζ changes its sign (Figure 13) our simulated flow field (Figure 10) here demonstrates a more realistic, smooth transition. As already shown for the surface charge pattern P1, the global relative error in the flow field associated with the no-slip violation soon becomes significant as the aspect ratio r_c/λ_D is reduced below 50. In this region ($r_c/\lambda_D < 100$) the slip-condition should be used with care concerning a numerical investigation of the EOF and resulting hydrodynamic dispersion. Consequently, this approximation does not appear useful in simulating flow through complex porous media with broad range of aspect ratios ($1 \approx r_c/\lambda_D \gg 1$), and the more general approach described in this work could be followed.

5. CONCLUSIONS AND OUTLOOK

We have presented a numerical method for three-dimensional simulation of EOF in microfluidic channels and devices. It is applicable to structures with arbitrary pore space morphology (including their geometry, as well as topology) and an arbitrary distribution of the electrokinetic potential at the solid–liquid interface. This also covers the existence of random pore-size distributions and, as a consequence, the possibility of finding any range of aspect ratios in a particular medium. Coupled hydrodynamic, electrostatic, and mass transport problems were solved. In this work, the hydrodynamic problem has been treated with the lattice-Boltzmann method. Straight capillaries were chosen as model systems due to the possibility of comparing simulated data with the analytical solution and results of other numerical simulations for simple system configurations, in the effort to present a basis for efficient modelling of

electrokinetic phenomena in more complex porous media. Good agreement was obtained for different benchmark cases.

It should be mentioned that, in general, a further increase in the numerical accuracy of the presented approach can be achieved without additional cost of computational time by an implementation of multiscale schemes, e.g. with locally embedded grids in which the lattice spacing is refined (or coarsened) locally. This approach allows to analyse the flow problem with a finer spatial resolution in regions characterized by larger velocity gradients and define more accurately curved interfaces [79–82]. However, EOF regions which require the imposition of finer computational grids cannot always be recognized *a priori* [83], and further work is needed for devising criteria to detect such regions of interest under a given set of conditions.

A low-Reynolds number EOF dynamics on micrometer scale is not only encountered in open-channel structures of microchip devices, but also in the voids of microscopically disordered media like random particulate packings or monoliths [59]. For example, in capillary electrochromatography, as for most microchip applications, EOF is employed for achieving significantly less dispersive transport (compared to pressure-driven flow) of complex mixtures of (bio)molecular species which are separated on the high-surface area materials to become identified afterwards, preferably by on-line detection, e.g. via mass spectrometry. Our numerical approach based on the lattice-Boltzmann flow field under most general conditions can cope with any geometry and surface heterogeneity, and it will be particularly efficient in resolving details of the flow field which govern mass transport and dispersion in a transient, as well as long-time asymptotic regime. For more complex porous media and flow patterns the presented approach can contribute to a derivation of scaling laws for the EOF, involving parameters such as the Reynolds and Peclet numbers, mass diffusivity, morphology of the medium, or electrical double layer thickness. However, this also stimulates further investigation of double layer resolution effects and limits when employing a slip-velocity boundary condition, in particular with respect to the characteristic lengths in a porous medium, e.g. the sphere or intraparticle pore diameter in fixed beds of porous spherical particles, continuously changing channel dimensions and a varying shape, or the spatio-temporal heterogeneity of local surface charge distributions.

ACKNOWLEDGEMENTS

We like to thank Prof. Dr Lutz Tobiska and Dr Walfred Grambow from the ‘Interdisziplinäres Zentrum für Paralleles Rechnen’ (Fakultät für Mathematik, Otto-von-Guericke-Universität Magdeburg, Germany) for their support, and Maxim Dautau (Department of System Analysis, Belarusian State University, Minsk, Belarus) for his help in scientific computing.

REFERENCES

1. Stone HA, Kim S. Microfluidics: basic issues, applications, and challenges. *AIChE Journal* 2001; **47**: 1250–1254.
2. Jensen KF. Microreaction engineering—is small better? *Chemical Engineering Science* 2001; **56**:293–303.
3. Giordano N, Cheng JT. Microfluidic mechanics: progress and opportunities. *Journal of Physics—Condensed Matter* 2001; **13**:R271–R295.
4. Whitesides GM, Stroock AD. Flexible methods for microfluidics. *Physics Today* 2001; **54**:42–49.
5. Chovan T, Guttman A. Microfabricated devices in biotechnology and biochemical processing. *Trends in Biotechnology* 2002; **20**:116–122.

6. Hessel V, Löwe H. Microtechnology: components—plant concepts—user acceptance. *Chemie-Ingenieur-Technik* 2002; **74**:185–207.
7. Reyes DR, Iossifidis D, Auroux PA, Manz A. Micro total analysis systems, 1. Introduction, theory, and technology. *Analytical Chemistry* 2002; **74**:2623–2636.
8. Probstein RF. *Physicochemical Hydrodynamics*. Wiley: New York, 1994; 190–202.
9. Hunter RJ. *Foundations of Colloid Science*. Oxford University Press: Oxford, 2001.
10. Rice CL, Whitehead R. Electrokinetic flow in a narrow cylindrical capillary. *Journal of Physical Chemistry* 1965; **69**:4017–4024.
11. Paul PH, Garguilo MG, Rakestraw DJ. Imaging of pressure- and electrokinetically-driven flows through open capillaries. *Analytical Chemistry* 1998; **70**:2459–2467.
12. Tallarek U, Rapp E, Scheenen T, Bayer E, Van As H. Electroosmotic and pressure-driven flow in open and packed capillaries: velocity distributions and fluid dispersion. *Analytical Chemistry* 2000; **72**:2292–2301.
13. Yang C, Li D, Masliyah JH. Modeling forced liquid convection in rectangular microchannels with electrokinetic effects. *International Journal of Heat and Mass Transfer* 1998; **41**:4229–4249.
14. Patankar NA, Hu HH. Numerical simulation of electroosmotic flow. *Analytical Chemistry* 1998; **70**:1870–1881.
15. Ermakov SV, Jacobson SC, Ramsey JM. Computer simulations of electrokinetic transport in microfabricated channel structures. *Analytical Chemistry* 1998; **70**:4494–4504.
16. Griffiths SK, Nilson RH. Hydrodynamic dispersion of a neutral nonreacting solute in electroosmotic flow. *Analytical Chemistry* 1999; **71**:5522–5529.
17. Bianchi F, Ferrigno R, Girault HH. Finite element simulation of an electroosmotic-driven flow division at a T-junction of microscale dimensions. *Analytical Chemistry* 2000; **72**:1987–1993.
18. Cummings EB, Griffiths SK, Nilson RH, Paul PH. Conditions for similitude between the fluid velocity and electric field in electroosmotic flow. *Analytical Chemistry* 2000; **72**:2526–2532.
19. Arulanandam S, Li D. Liquid transport in rectangular microchannels by electroosmotic pumping. *Colloids and Surfaces A* 2000; **161**:89–102.
20. Santiago JG. Electroosmotic flows in microchannels with finite inertial and pressure forces. *Analytical Chemistry* 2001; **73**:2353–2365.
21. Dutta P, Beskok A. Analytical solution of combined electroosmotic/pressure driven flows in two-dimensional straight channels: finite Debye layer effects. *Analytical Chemistry* 2001; **73**:5097–5102.
22. Yang RJ, Fu LM, Lin YC. Electroosmotic flow in microchannels. *Journal of Colloid and Interface Science* 2001; **239**:98–105.
23. Keh HJ, Tseng HC. Transient electrokinetic flow in fine capillaries. *Journal of Colloid and Interface Science* 2001; **242**:450–459.
24. Dutta P, Beskok A, Warburton TC. Electroosmotic flow control in complex microgeometries. *Journal of Microelectromechanical Systems* 2002; **11**:36–43.
25. Fu LM, Yang RJ, Lee GB. Analysis of geometry effects on band spreading of microchip electrophoresis. *Electrophoresis* 2002; **23**:602–612.
26. Kang YJ, Yang C, Huang XY. Electroosmotic flow in a capillary annulus with high zeta-potentials. *Journal of Colloid and Interface Science* 2002; **253**:285–294.
27. Erickson D, Li D. Influence of surface heterogeneity on electrokinetically driven microfluidic mixing. *Langmuir* 2002; **18**:1883–1892.
28. Conlisk AT, McFerran J, Zheng Z, Hansford D. Mass transfer and flow in electrically charged micro- and nanochannels. *Analytical Chemistry* 2002; **74**:2139–2150.
29. Frisch U, d'Humieres D, Hasslacher B, Lallemand P, Pomeau Y, Rivet JP. Lattice gas hydrodynamics in two and three dimensions. *Complex Systems* 1987; **1**:649–707.
30. McNamara G, Zanetti G. Use of the Boltzmann equation to simulate lattice-gas automata. *Physical Review Letters* 1988; **61**:2332–2335.
31. Higuera FJ, Jiménez J. Boltzmann approach to lattice gas simulations. *Europhysics Letters* 1989; **9**:663–668.
32. Succi S, Benzi R, Higuera F. The lattice-Boltzmann equation—a new tool for computational fluid dynamics. *Physica D* 1991; **47**:219–230.
33. Benzi R, Succi S, Vergassola M. The lattice Boltzmann equation—theory and applications. *Physics Reports* 1992; **222**:145–197.
34. Chen S, Doolen GD. Lattice Boltzmann method for fluid flows. *Annual Review of Fluid Mechanics* 1998; **30**:329–364.
35. Spaid MAA, Phelan FR Jr. Lattice Boltzmann methods for modeling microscale flow in fibrous porous media. *Physics of Fluids* 1997; **9**:2468–2474.
36. Maier RS, Kroll DM, Kutsovsky YE, Davis HT, Bernard RS. Simulation of flow through bead packs using the lattice Boltzmann method. *Physics of Fluids* 1998; **10**:60–74.
37. Manz B, Gladden LF, Warren PB. Flow and dispersion in porous media: lattice-Boltzmann and NMR studies. *AIChE Journal* 1999; **45**:1845–1854.

38. Maier RS, Kroll DM, Davis HT, Bernard RS. Simulation of flow in bidisperse sphere packings. *Journal of Colloid and Interface Science* 1999; **217**:341–347.
39. Bernsdorf J, Brenner G, Durst F. Numerical analysis of the pressure drop in porous media flow with lattice Boltzmann (BGK) automata. *Computer Physics Communications* 2000; **129**:247–255.
40. Clague DS, Kandhai BD, Zhang R, Sloot PMA. Hydraulic permeability of (un)bounded fibrous media using the lattice Boltzmann method. *Physical Review E* 2000; **61**:616–625.
41. Hill RJ, Koch DL, Ladd AJC. Moderate-Reynolds-number flows in ordered and random arrays of spheres. *Journal of Fluid Mechanics* 2001; **448**:243–278.
42. Békri S, Vizika O, Thovert JF, Adler PM. Binary two-phase flow with phase change in porous media. *International Journal of Multiphase Flow* 2001; **27**:477–526.
43. Drazer G, Koplik J. Tracer dispersion in two-dimensional rough fractures. *Physical Review E* 2001; **63**:art. no. 056104.
44. Maier RS, Kroll DM, Bernard RS, Howington SE, Peters JF, Davis HT. Enhanced dispersion in cylindrical packed beds. *Philosophical Transactions of the Royal Society of London A* 2002; **360**:497–506.
45. Yoshino M, Inamuro T. Lattice Boltzmann simulations for flow and heat/mass transfer problems in a three-dimensional porous structure. *International Journal for Numerical Methods in Fluids* 2003; **43**:183–198.
46. Kandhai D, Hlushkou D, Hoekstra AG, Sloot PMA, Van As H, Tallarek U. Influence of stagnant zones on transient and asymptotic dispersion in macroscopically homogeneous porous media. *Physical Review Letters* 2002; **88**:art. no. 234501.
47. Schure MR, Maier RS, Kroll DM, Davis HT. Simulation of packed-bed chromatography utilizing high-resolution flow fields: comparison with models. *Analytical Chemistry* 2002; **74**:6006–6016.
48. Kang QH, Zhang DX, Chen SY. Unified lattice Boltzmann method for flow in multiscale porous media. *Physical Review E* 2002; **66**:art. no. 056307.
49. Zeiser T, Steven M, Freund H, Lammers P, Brenner G, Durst F, Bernsdorf J. Analysis of the flow field and pressure drop in fixed-bed reactors with the help of lattice Boltzmann simulations. *Philosophical Transactions of the Royal Society of London A* 2002; **360**:507–520.
50. Békri S, Howard J, Muller J, Adler PM. Electrical resistivity index in multiphase flow through porous media. *Transport in Porous Media* 2003; **51**:41–65.
51. Bhatnagar P, Gross E, Krook M. A model for collision processes in gases: I. small amplitude processes in charged and neutral one-component systems. *Physical Review* 1954; **94**:511–525.
52. Chen S, Chen H, Martinez D, and Matthaeus WH. Lattice Boltzmann model for simulation of magnetohydrodynamics. *Physical Review Letters* 1991; **67**:3776–3779.
53. Qian YH, d'Humieres D, Lallemand P. Lattice BGK models for the Navier–Stokes equation. *Europhysics Letters* 1992; **17**:479–484.
54. Li B, Kwok DY. Lattice Boltzmann model of microfluidics with high Reynolds numbers in the presence of external forces. *Langmuir* 2003; **19**:3041–3048.
55. Ren L, Qu W, Li D. Interfacial electrokinetic effects on liquid flow in microchannels. *International Journal of Heat and Mass Transfer* 2001; **44**:3125–3134.
56. Nie X, Doolen GD, Chen S. Lattice-Boltzmann simulations of fluid flows in MEMS. *Journal of Statistical Physics* 2002; **107**:279–289.
57. Warren PB. Electroviscous transport problems via lattice-Boltzmann. *International Journal of Modern Physics C* 1997; **8**:889–898.
58. Gross RJ, Osterle JF. Membrane transport characteristics of ultrafine capillaries. *Journal of Chemical Physics* 1968; **49**:228–234.
59. Rathore AS. Theory of electroosmotic flow, retention and separation efficiency in capillary electro-chromatography. *Electrophoresis* 2002; **23**:3827–3846.
60. Tallarek U, Rapp E, Seidel-Morgenstern A, Van As H. Electroosmotic flow phenomena in packed capillaries: from the interstitial velocities to intraparticle and boundary layer mass transfer. *Journal of Physical Chemistry B* 2002; **106**:12709–12721.
61. Ren L, Li D. Electroosmotic flow in heterogeneous microchannels. *Journal of Colloid and Interface Science* 2001; **243**:255–261.
62. Coelho D, Shapiro M, Thovert JF, Adler PM. Electroosmotic phenomena in porous media. *Journal of Colloid and Interface Science* 1996; **181**:169–190.
63. Kandhai D, Koponen A, Hoekstra AG, Kataja M, Timonen J, Sloot PMA. Implementation aspects of 3D lattice-BGK: boundaries, accuracy, and a new fast relaxation method. *Journal of Computational Physics* 1999; **150**:482–501.
64. Guo Z, Zheng C, Shi B. Discrete lattice effects on the forcing term in the lattice Boltzmann method. *Physical Review E* 2002; **65**:art. no. 046308.
65. Hiemenz PC, Rajagopalan R. *Principles of Colloid and Surface Chemistry*. Marcel Dekker: New York, 1997.
66. Delgado AV, Arroyo FJ. Electrokinetic phenomena and their experimental determination: an overview. In *Interfacial Electrokinetics and Electrophoresis*, Delgado AV (ed.). Marcel Dekker: New York, 2002.

67. Anderson JL, Idol WK. Electroosmosis through pores with nonuniformly charged walls. *Chemical Engineering Communications* 1985; **38**:93–106.
68. Potoček B, Gaš B, Kenndler E, Štědrý M. Electroosmosis in capillary zone electrophoresis with nonuniform zeta-potential. *Journal of Chromatography A* 1995; **709**:51–62.
69. Weidenhammer P, Jacobasch HJ. Investigation of adhesion properties of polymer materials by atomic force microscopy and zeta-potential measurements. *Journal of Colloid and Interface Science* 1996; **180**:232–236.
70. Hayes RA. The electrokinetic behaviour of surfaces modified by particle adsorption. *Colloids and Surfaces A* 1999; **146**:89–94.
71. Herr AE, Molho JI, Santiago JG, Mungal MG, Kenny TW, Garguilo MG. Electroosmotic capillary flow with nonuniform zeta potential. *Analytical Chemistry* 2000; **72**:1053–1057.
72. Ghosal S. Lubrication theory for electro-osmotic flow in a microfluidic channel of slowly varying cross-section and wall charge. *Journal of Fluid Mechanics* 2002; **459**:103–128.
73. Pačes M, Kosek J, Marek M, Tallarek U, Seidel-Morgenstern A. Mathematical modelling of adsorption and transport processes in capillary electrochromatography: open–tubular geometry. *Electrophoresis* 2003; **24**:380–389.
74. Long D, Stone HA, Ajdari A. Electroosmotic flows created by surface defects in capillary electrophoresis. *Journal of Colloid and Interface Science* 1999; **212**:338–349.
75. Regnier FE, Wu D. Chemical derivatization of fused silica capillaries. In *Capillary Electrophoresis Technology*, Guzman NA (ed.). Marcel Dekker: New York, 1993; 287–309.
76. Stroock AD, Weck M, Chiu DT, Huck WTS, Kenis PJA, Ismagilov RF, Whitesides GM. Patterning electroosmotic flow with patterned surface charge. *Physical Review Letters* 2000; **84**:3314–3317.
77. Ajdari A. Generation of transverse fluid currents and forces by an electric field: electro-osmosis on charge-modulated and undulated surfaces. *Physical Review E* 1996; **53**:4996–5005.
78. Gleeson JP. Electroosmotic flows with random zeta-potential. *Journal of Colloid and Interface Science* 2002; **249**:217–226.
79. Peng Y, Shu C, Chew YT, Inamuro T. Lattice kinetic scheme for the incompressible viscous thermal flows on arbitrary meshes. *Physical Review E* 2004; **69**:art. no. 016703.
80. Filippova O, Hänel D. Grid refinement for lattice-BGK models. *Journal of Computational Physics* 1998; **147**:219–228.
81. Filippova O, Schwade B, Hänel D. Multiscale lattice Boltzmann schemes for low Mach number flows. *Philosophical Transactions of the Royal Society of London A* 2002; **360**:467–476.
82. Yu D, Mei R, Luo L-S, Shyy W. Viscous flow computations with the method of lattice Boltzmann equation. *Progress in Aerospace Sciences* 2003; **39**:329–367.
83. Hlushkou D. Numerical simulation of flow and mass transport in (electro-) chromatographic systems. *Ph.D. Thesis*, Otto-von-Guericke-Universität Magdeburg, Germany, 2004.

